Accurate Persistent Scatterer Identification Based on Phase Similarity of Radar Pixels

Ke Wang and Jingyi Chen, *Member, IEEE*

***Abstract*— Phase decorrelation, caused by changes in the surface scattering properties between two radar acquisitions, is a major limiting factor for interferometric synthetic aperture radar (InSAR) surface deformation analysis over vegetated terrain. Persistent Scatterer (PS) techniques have been developed to identify high-quality radar pixels suffering from minimal decorrelation artifacts. However, existing PS selection algorithms are often based on the statistics of InSAR amplitude and phase measurements at each individual radar pixel, and scattering signal models that take into account the phase correlation of nearby PS pixels have not been fully developed. Here, we present a new PS selection algorithm based on the similarity of phase observations between nearby radar pixels. We used this algorithm to analyze 25 C-band Envisat SAR scenes acquired over the San Luis Valley, Colorado, and 93 C-band Sentinel-1 SAR scenes acquired over the Greater Houston area, Texas. At both the test sites, the presence of dense vegetation leads to severe phase decorrelation artifacts even in some interferograms with short temporal baselines. Our algorithm can reduce the number of false positive and false negative PS pixels identified from an existing PS identification algorithm. The improved PS identification accuracy allows us to substantially increase the total number of high-quality interferograms that are suitable for time series analysis. We reconstructed spatially coherent InSAR phase observations through an interpolation between PS pixels, and recovered subtle deformation signals that are otherwise undetectable. In both the cases, the superior performance of our PS processing strategy was demonstrated using a large number of independent ground-truth data.**

***Index Terms*— Decorrelation, Interferometric Synthetic Aperture Radar (InSAR), Persistent Scatterer (PS), phase similarity, surface deformation.**

I. Introduction

RECENT satellite missions have been collecting interferometric synthetic aperture radar (InSAR) [1], [2] data over the entire world on very short revisit cycles (e.g., six days for Sentinel-1 with a two-satellite constellation). However, mapping centimeter-to-millimeter surface deformation (e.g., [3], [4], [5], [6], [7], [8], [9], [10], [11], [12]) on a global scale is challenging. One major limitation is that a substantial portion of the world's land surface is covered by vegetation, and vegetation growth between consecutive radar acquisitions leads to changes in surface scattering properties and decorrelation in InSAR phase measurements [13]. InSAR phase measurements at decorrelated radar pixels can be considered as random wrapped phase values between 0 and 2π, and they cannot be used to reconstruct spatially coherent phase components such as surface deformation signals and tropospheric noise signatures. To overcome this limitation, persistent scatterer (PS) techniques (e.g., [14], [15], [16]) have been developed to identify radar pixels with stable surface scattering properties (e.g., man-made structures, rocks, and barren lands). In areas with dense vegetation, only phase measurements at PS pixels have a high quality that is suitable for time series analysis.

The first generation of PS algorithms [17], [18], [19] modeled radar echoes as the sum of a constant real signal and a complex circular Gaussian random noise. Based on this model, the returns from a radar pixel with a high signal-to-noise ratio (SNR) have relatively small amplitude variations. A pixel with high amplitude stability is identified as a PS pixel if its phase observations fit a given deformation model. One limitation of such approaches is that there are typically very few radar pixels with sufficient SNRs to be selected in natural terrain. To overcome this limitation, [15], [20], [21], [22] select PS pixels based on the statistics of InSAR phase measurements. Using a complex circular Gaussian model for both the signal and noise terms, Shanker and Zebker [21] estimated the signal-to-clutter ratio (SCR) of each radar pixel using phase measurements of interferograms that share a common reference SAR image. A PS pixel is expected to have relatively a high SCR and a narrow phase distribution. The capability of PS interferometry was further advanced by the SqueeSAR method [16], [23], [24]. Ferretti et al. [16] jointly analyzed the nearby pixels with homogeneous amplitude distributions (these pixels are referred to as Statistically Homogeneous Pixels or SHP in [16]). InSAR phase observations from each SHP group are averaged to improve the SNR, and a covariance matrix model [25] is used to filter phase measurements and select PS pixels. The SqueeSAR-based approach is one of the very few existing methods that take into account the amplitude statistics of nearby distributed scatterers (DSs). Alternatively, Costantini et al. [26], [27] modeled the phase difference between two adjacent radar pixels as a function of the deformation rate difference and elevation difference. For each neighboring pixel pair, an optimized deformation rate difference and elevation difference are solved to minimize the residual phase difference. The pixel pair is selected as PS if the residual phase difference is small.

Because scattering signal models that take into account the phase correlation of nearby PS pixels have not been fully developed [28], existing PS selection algorithms are

Manuscript received 23 April 2022; revised 3 July 2022 and 23 August 2022; accepted 25 September 2022. Date of publication 28 September 2022; date of current version 24 October 2022. This work was supported by the Future Investigators in NASA Earth and Space Science and Technology Program under Grant 80NSSC20K1621. Jingyi Chen was supported by the NASA Earth Surface and Interior Program under Grant 80NSSC18K0467 and Grant 80NSSC22K0412. *(Corresponding authors: Ke Wang; Jingyi Chen.)*

The authors are with the Department of Aerospace Engineering and Engineering Mechanics, Cockrell School of Engineering, University of Texas at Austin, Austin, TX 78712 USA (e-mail: kewang@utexas.edu; jingyi.ann.chen@utexas.edu).

This article has supplementary downloadable material available at https://doi.org/10.1109/TGRS.2022.3210868, provided by the authors.

Digital Object Identifier 10.1109/TGRS.2022.3210868

mainly based on the statistics of InSAR phase measurements at each individual radar pixel. In many cases, a deformation model (e.g., constant velocity) is used in the selection process. However, surface deformation characteristics over an area of interest are often unknown. To overcome these limitations, here we present a new PS selection method that analyzes the phase correlation of nearby radar pixels based on a similarity measure (the cosine similarity). Our algorithm can be used alone for PS identification, or it can be integrated with any existing PS selection algorithm to reduce the false positive and false negative PS selections at a very low computational cost. By taking into account the varying decorrelation noise in different interferograms, our algorithm selects a unique PS set for each interferogram, which maximizes the number of high-quality radar measurements that can be used for surface deformation analysis. We applied this algorithm to analyze: 1) 25 C-band Envisat SAR scenes acquired over the San Luis Valley (SLV), Colorado, where confined aquifer pumping and recharge causes seasonal deformation over the agricultural basin and 2) 93 C-band Sentinel-1 SAR scenes acquired over the Greater Houston area, Texas, where long-term coastal subsidence increases the flooding risk in both the densely populated city center and the rural communities. We reconstructed the spatial coherent phase measurements associated with deformation signals and tropospheric noise signatures in areas with very low PS density (<10%) through a PS-based phase interpolation. Following this new PS processing strategy, the number of interferograms with quality suitable for time series analysis is substantially increased. Using this new algorithm, it is now feasible to achieve similar surface deformation mapping accuracy in densely vegetated terrain as in urban areas with very high PS density.

II. Methodology

A. Algorithm

Given K single-look complex (SLC) radar images $S_1, \ldots, S_K$, we can form $K-1$ wrapped interferograms that share a common reference SLC image. The phase values of these $K-1$ interferograms at a pixel m can be written as a phase vector $\boldsymbol{\varphi}_m = [\varphi_{m,1}, \varphi_{m,2}, \ldots, \varphi_{m,K-1}]$. We define the phase similarity between two radar pixels m and n as the cosine similarity between the phase vectors $\boldsymbol{\varphi}_m$ and $\boldsymbol{\varphi}_n$

$$s_{mn} = \frac{1}{K-1}\sum_{k=1}^{K-1}\cos\left(\varphi_{m,k} - \varphi_{n,k}\right). \tag{1}$$

Here, the phase similarity score s_{mn} ranges from -1 to 1. A similarity score of 1 means $\boldsymbol{\varphi}_m$ and $\boldsymbol{\varphi}_n$ are identical, 0 means $\boldsymbol{\varphi}_m$ and $\boldsymbol{\varphi}_n$ are not correlated, and -1 means $\varphi_{m,k}$ and $\varphi_{n,k}$ differ by π rad for all ks. We choose to use the cosine similarity rather than the temporal coherence [15]

$$\rho_{mn} = \frac{1}{K-1}\left|\sum_{k=1}^{K-1}\exp\left[i\left(\varphi_{m,k} - \varphi_{n,k}\right)\right]\right| \tag{2}$$

as the similarity measure of two phase vectors, which allows us to better capture phase errors in the reference SLC image. For example, consider a case that: 1) the SAR phase measurements at pixel m and n differ by $\pi/2$ rad in the reference SAR image S_k because of a random decorrelation error and 2) the SAR phase measurements at these two pixels are identical in the rest of the SAR images without any phase errors. Such phase error in the reference image can cause a constant phase offset of $\pi/2$ rad between the two InSAR phase vectors $\boldsymbol{\varphi}_m$ and $\boldsymbol{\varphi}_n$. In this case, the cosine similarity (1) can detect the inconsistency between $\boldsymbol{\varphi}_m$ and $\boldsymbol{\varphi}_n$ by returning a similarity score of 0, while the temporal coherence (2) overestimates their similarity by returning 1.

Our algorithm is designed to retrieve accurate deformation signals over low PS density natural terrains. In this scenario, the deformation signal of interest is often caused by geophysical processes, including but not limited to coastal processes, aquifer pumping and recharge, volcanism, or fault activities. Because the Earth's crust can be modeled as a solid continuum, such surface displacements typically vary slowly in space [29]. Given that the deformation signal of interest and tropospheric noise are both spatially coherent, phase vectors of two nearby PS pixels are expected to be similar (e.g., with phase similarity >0.5). In contrast, the similarity score of a decorrelated pixel (a non-PS pixel) and a nearby pixel is ∼0 when the total number of SAR acquisitions K is sufficiently large. This is because the phase of a decorrelated pixel can be considered as a random value between 0 and 2π [13].

It is computationally expensive to calculate the phase similarity between all the radar pixel pairs. To improve computational efficiency, we first select a set of PS candidate pixels using the maximum likelihood estimation (MLE) selection technique described in [21]. Following [21], the received echo from a radar pixel can be modeled as a coherent sum of returns from a dominant scatterer and clutter scatterers, and both the components are considered as circular complex Gaussian random variables. The relative power of the dominant scatterer signal to the background clutter noise is defined as the SCR (γ). Based on this model, the probability density function (PDF) of the observed InSAR phase φ for a given SCR γ can be written as

$$p(\varphi|\gamma) = \frac{1-\rho^2}{2\pi}\frac{1}{1-\rho^2\cos^2\varphi} \times\left(1+\frac{\rho\cos\varphi\arccos(-\rho\cos\varphi)}{\sqrt{1-\rho^2\cos^2\varphi}}\right) \tag{3}$$

where ρ is defined as $\rho = 1/(1+\gamma^{-1})$. A PS pixel has a high SCR and a relatively narrow phase distribution, while a non-PS pixel has a low SCR and a relatively wide phase distribution. We estimate the SCR value $\hat{\gamma}_{\mathrm{ML},m}$ at a given pixel m by comparing the observed InSAR phase vector $\boldsymbol{\varphi}_m$ to (3) in a maximum likelihood sense

$$\hat{\gamma}_{\mathrm{ML},m} = \arg\max_{\gamma}\prod_{k=1}^{K-1} p\left(\tilde{\varphi}_{m,k}|\gamma\right) \tag{4}$$

where $\tilde{\varphi}_{m,k}$ is the residual phase at pixel m in the kth interferogram after removing the spatially correlated phase component through filtering. We classified PS candidates as the pixels with $\hat{\gamma}_{\mathrm{ML},m} > 2$. This threshold value was suggested by previous SCR-based PS selection studies [21], [22], [30],

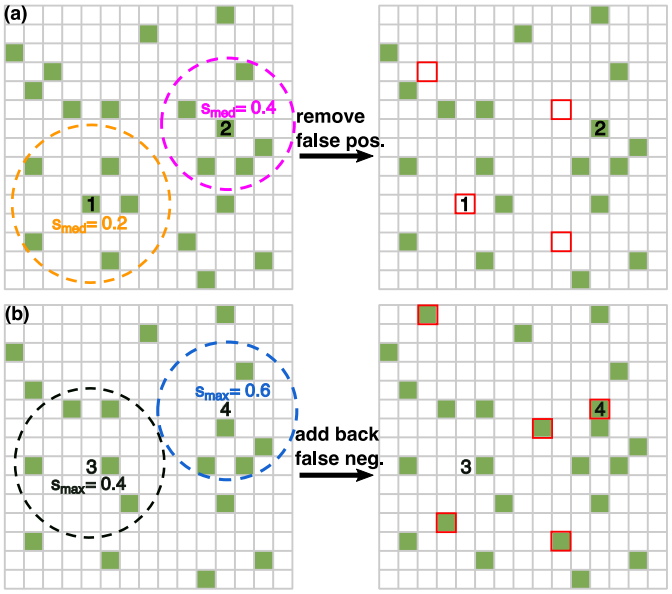

Fig. 1. PS selection algorithm based on the similarity of phase vectors. (a) Remove false positive detections from preliminary PS candidates. For each PS candidate (green pixels), we calculate its median phase similarity with its N nearest neighbor PS candidates. PS candidates with a median phase similarity score lower than 0.3 are removed. (b) Identify false negative detections and expand the PS set. For each non-PS pixel (white pixels), we calculate its maximum phase similarity with the N nearest neighbor PS candidates. Pixels with a maximum phase similarity score greater than a predetermined threshold (0.5 in this example) are selected as new PS pixels.

[31] as a reasonable trade-off between the false positive and false negative rates. A higher $\hat{\gamma}_{\mathrm{ML},m}$ value leads to a lower false positive rate and a higher false negative rate.

During preliminary PS candidate selection, the SCR value at each pixel is estimated independently. The spatial phase consistency between PS pixels is not taken into account, which may lead to inaccurate PS selections [31]. To overcome this limitation, we next identify and remove false positive PS pixels based on the phase similarity between PS candidate pixels as follows. Given a PS candidate pixel m, we calculate its phase similarity with its N nearest neighbor PS candidates [Fig. 1(a)]. We define the median value of these N phase similarity measurements $s_{\mathrm{med},m}$ as

$$s_{\mathrm{med},m} = \underset{n\in \mathrm{NN}(m,N)}{\mathrm{median}}\, s_{mn} \tag{5}$$

where $\mathrm{NN}(m, N)$ represents the N nearest neighbor PS candidates of pixel m. The value of N needs to be sufficiently large to be statistically meaningful, while pixels in $\mathrm{NN}(m, N)$ need to be adequately close to each other so that they contain a similar phase signal. In this study, we set $N = 20$ as a trade-off between these two considerations, and we remove PS candidates with median phase similarity values less than $s_{\mathrm{med,thr}} = 0.3$.

To further recover false negatives in the preliminary PS candidate selection, we calculate the phase similarity of every non-PS pixel m with its N nearest neighbor PS pixels [Fig. 1(b)] as

$$s_{\mathrm{max},m} = \max_{n\in \mathrm{NN}(m,N)} s_{mn} \tag{6}$$

where $\mathrm{NN}(m, N)$ represents the N nearest neighbor PS pixels of pixel m. The pixel m is selected as a new PS if the maximum phase similarity is greater than a predefined threshold $s_{\mathrm{max,thr}}$. The search of false negative PS pixels is performed iteratively to expand the PS set, and the number of PS pixels increases monotonically through iterations. Because the number of detected PS pixels is upper bounded by the total number of radar pixels, our algorithm is guaranteed to terminate when no more PS pixels can be identified through additional iterations. Because the phase vectors of two non-PS pixels are unlikely to be similar when the number of SAR acquisitions is sufficiently large (e.g., $K > 50$), the search for false negatives typically introduces very few false positive PS pixels.

To determine the similarity threshold $s_{\mathrm{max,thr}}$, we compute the phase correlation of each interferogram [13], and we use pixels with the lowest 1% average InSAR phase correlation as calibration pixels (e.g., decorrelated non-PS pixels such as water, cultivated land, or forest pixels). Alternatively, water pixels from a land-cover classification map [32], [33] can be used as calibration pixels. For each calibration pixel m, we calculate its maximum phase similarity with the nearby pixels as

$$\tilde{s}_{\mathrm{max},m} = \max_{n\in B(m,r)} s_{mn} \tag{7}$$

where $B(m, r)$ represents the set of pixels in a circle centered at pixel m (with pixel m itself excluded). The radius of the circle needs to be sufficiently large to be statistically meaningful, while all the pixels need to be adequately close to each other so that the phase vectors at PS pixels are similar. In this study, the circle radius r is set to 50 pixels. The similarity threshold $s_{\mathrm{max,thr}}$ is chosen so that the probability of selecting a calibration pixel as PS (false positive) is below 1% (defined as the probability threshold $\alpha = 1\%$).

Our PS selection algorithm is illustrated as a flowchart (Fig. 2). We emphasize that the choice of reference SLC images influences PS pixel selection. For example, if a radar pixel contains substantial phase noise in the reference SLC image, it is likely marked as a non-PS pixel because all the interferograms that share this reference SLC are corrupted by this phase noise. As a result, given K SLC images, we choose each of them as a unique reference SLC image and derive K corresponding PS sets $\Omega_1, \ldots, \Omega_K$. We use the intersection of two PS sets $\Omega_k \cap \Omega_l$ as the valid PS set for the interferogram formed between SAR image S_k and S_l. Our algorithm takes into account that the quality of an interferogram is determined by two SAR scenes, and the number of high-quality PS pixels can vary substantially among different interferograms. This allows us to improve the overall efficiency and accuracy of our detections (see Section V-A).

B. Validate PS Selection Through PS Interpolation

Our algorithm identifies high-quality InSAR phase measurements at a set of isolated PS pixels. To reconstruct spatially coherent phase observations (including deformation signals and tropospheric noise), we use an adaptive spatial interpolation between PS pixels as proposed in [34]. Given a wrapped interferogram, the phase value at pixel m is replaced

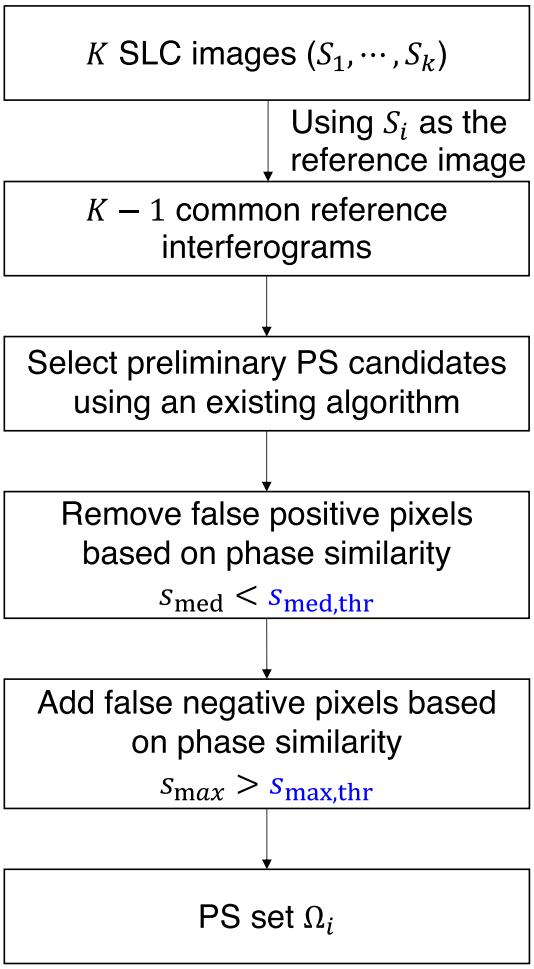

Fig. 2. Flowchart of the phase similarity PS identification algorithm. We consider $\Omega_k \cap \Omega_l$ as the valid PS set for the interferogram formed using SLCs S_k and S_l. We recommend 0.3 as the default value for the median phase similarity threshold $s_{\text{med,thr}}$. The maximum phase similarity threshold $s_{\text{max,thr}}$ can be calculated based on the maximum acceptable probability of selecting pixels with random phases (see Section II-A). Users can also specify these two thresholds if necessary to improve the PS selection accuracy.

by the weighted average phase value of its N nearest neighbor PS pixels as

$$\varphi_m^{\text{interp}} = \arg\left(\sum_{n\in \text{NN}(m,N)} w_n e^{i\varphi_n}\right) \tag{8}$$

where $\arg(z)$ is the argument of the complex number z, $\text{NN}(m, N)$ represents the N nearest neighbor PS pixels of pixel m, and φ_n is the wrapped phase value at pixel n. $w_n = e^{-r_n^2/2R}$, where r_n is the distance between the center pixel m and the pixel n and $R = \max_n r_n$.

Using the PS interpolation method, we can fill the spatial gaps in high-quality InSAR phase measurements. Also, it is much easier to unwrap a PS-interpolated interferogram than a decorrelated interferogram. For example, it takes on average 1 min to interpolate a 2000-by-2000 pixel interferogram and another 10 s to unwrap the interpolated interferogram using the statistical-cost, network-flow algorithm for phase unwrapping (SNAPHU) algorithm [35]. Without PS interpolation, unwrapping a severely decorrelated interferogram of the same size can take more than 2 h on the same machine. Therefore, interpolating interferograms before phase unwrapping can greatly improve the computational efficiency of InSAR data processing at large scales.

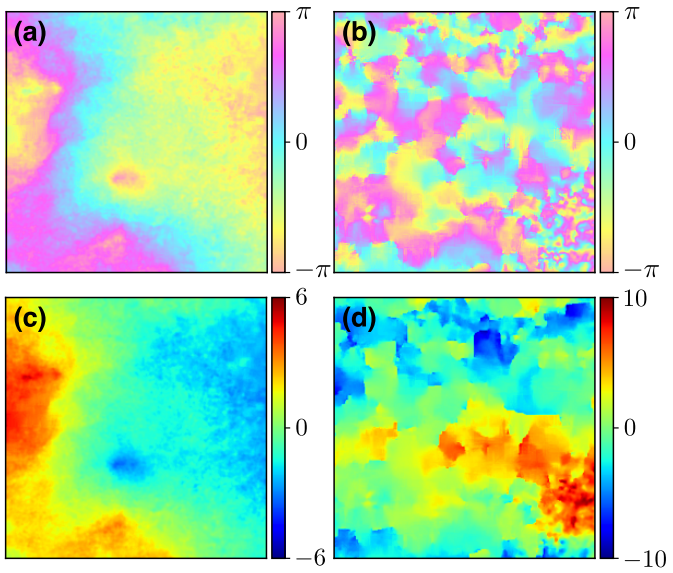

Fig. 3. Examples of PS-interpolated wrapped Sentinel-1 interferograms with (a) few interpolation artifacts and (b) severe interpolation artifacts. (c) Phase unwrapping result of Panel (a). (d) Phase unwrapping results of Panel (b). Following (9), the phase unwrapping error is 0 and 17134.3 rad for (c) and (d), respectively.

In addition, we use PS interpolation to evaluate the accuracy of PS selection (e.g., Fig. 3). While accurate PS selection usually results in spatially smooth phase reconstruction, interpolation from inaccurate PS sets can cause abrupt phase changes near false positive PS pixels. Such phase artifacts can be easily identified through visual inspection, which gives a qualitative measure of PS selection accuracy. Alternatively, we can unwrap the interpolated interferogram and quantify the interpolation artifacts as phase unwrapping errors. Given an unwrapped interpolated interferogram, we define the phase unwrapping error at a radar pixel m as

$$\varphi_m^{\text{err}} = \sum_n |\Delta\varphi_{mn}| f_\pi(|\Delta\varphi_{mn}|) \tag{9}$$

where $\Delta\varphi_{mn}$ is the unwrapped phase difference between pixel m and pixel n (or $\varphi_m^{\text{unwrap}} - \varphi_n^{\text{unwrap}}$), f_π being an indicator function such that $f_\pi(x) = 1$ if $x > \pi$, and $f_\pi(x) = 0$ otherwise. The summation is performed on four adjacent pixels of the center pixel m. We calculate the total phase unwrapping error of an interferogram by summing up the phase unwrapping error over all the radar pixels. If the phase difference between any pair of adjacent pixels is less than π rad, the total phase unwrapping error is 0. Interferograms with total phase unwrapping errors above a threshold are excluded from InSAR time series analysis.

III. Test Sites and InSAR Analysis

A. San Luis Valley (SLV)

The SLV is an agricultural basin in southern Colorado, where confined aquifer pumping has caused surface deformation detectable by InSAR [31], [36], [37], [38]. InSAR analysis is challenging over vegetated terrain, where deformation signals can be easily obscured by decorrelation noise. Chen et al. [31] applied a PS selection algorithm (known as the

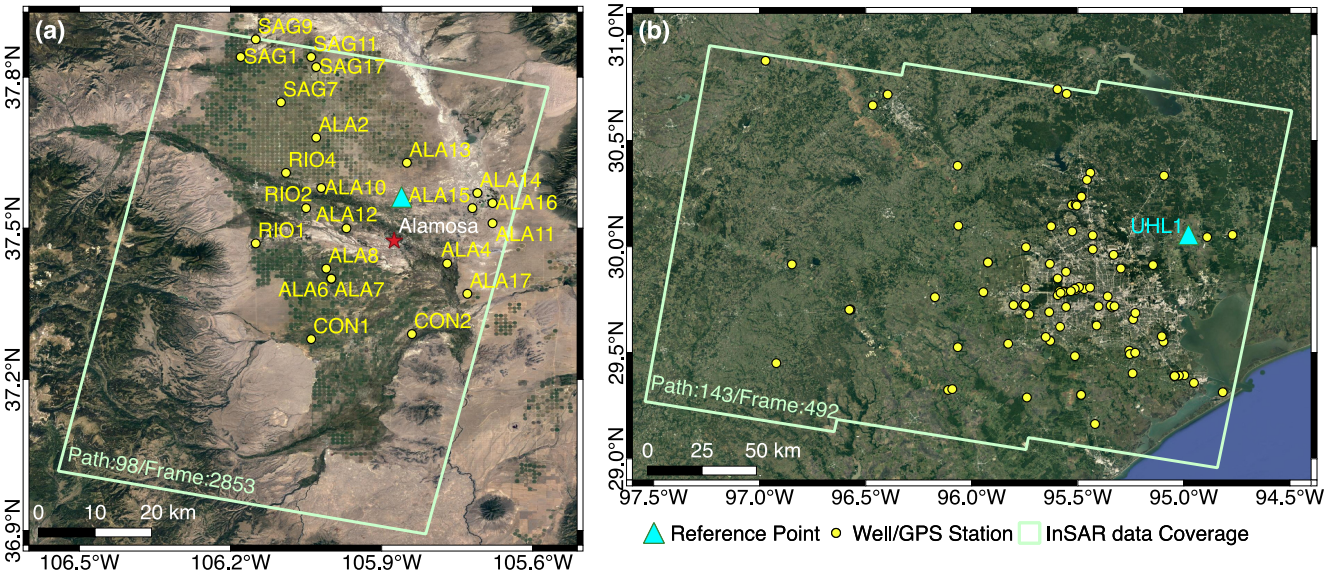

Fig. 4. (a) SLV, Colorado. The Envisat spatial coverage over the study site is outlined in light green. Yellow dots represent the locations of the 23 long-term confined aquifer monitoring wells. The cyan triangle represents the reference point of all the interferograms. (b) Greater Houston area, Texas. The Sentinel-1 spatial coverage over the study site is outlined in light green. Yellow dots represent the locations of the 93 GPS stations that were jointly analyzed with Sentinel-1 data. The cyan triangle represents the reference point of the interferograms, which is colocated with the GPS station UHL1.

MLE algorithm) described in [21], and processed 25 C-band Envisat SLC images (Path 98 and Frame 2853) acquired between November 20, 2006 and July 12, 2010 [Fig. 4(a)]. They estimated the SCR value at each pixel using interferograms that share a common reference Envisat scene acquired on November 09, 2009. The reference scene was chosen to maximize the average InSAR phase correlation of the common reference interferograms as suggested in [21].

We also identified PS pixels using the new phase similarity algorithm. We denote Ω_k as the PS set associated with the kth reference SLC scene. Because the phase noise level of the reference SLC image greatly influences the phase similarity score, the selected 25 PS sets from different reference SLCs are typically not identical (Fig. 5). The common PS pixels in Ω_k and Ω_l (or $\Omega_k \cap \Omega_l$) were considered as the valid PS pixels for the interferogram formed using the kth and the lth SLCs. We note that the MLE algorithm identifies a pixel as PS if its SCR value is greater than a certain threshold. While a higher SCR threshold reduces false positives, it increases false negatives and underestimates the PS density. Similarly, a lower SCR threshold increases false positives, but reduces false negatives. To ensure a fair comparison between the two algorithms, we set the SCR threshold so that both the algorithms select approximately the same number of PS pixels for each interferogram. We consider a PS selection algorithm is better if it can reconstruct spatially coherent interferograms with fewer PS interpolation artifacts and smaller unwrapping errors (9).

To perform the InSAR time series analysis, we interpolated all 300 interferograms based on the PS pixels identified from the phase similarity algorithm. We excluded 78 interferograms (typically with large spatial or temporal baselines) containing obvious interpolation or unwrapping artifacts. The remaining 222 interferograms were unwrapped and referenced to a point northeast of Alamosa, CO, which is far away from the primary confined aquifer pumping region. We removed an empirical linear phase ramp in each unwrapped interferogram to account for potential atmospheric noise or orbital error. We solved for the line-of-sight (LOS) deformation rate between consecutive Envisat SAR acquisition at each radar pixel using the unconstrained least-squares small baseline subset (SBAS) algorithm [39]. We integrated the deformation rate to reconstruct the LOS deformation time series. Under the assumption that there were no substantial horizontal deformation signals, we converted the LOS deformation into vertical deformation. We jointly analyzed InSAR vertical deformation series and head levels recorded at 22 out of 23 long-term confined aquifer monitoring wells [Fig. 4(a)]. We excluded well ALA12 from the analysis, because the head records were too noisy to capture the seasonal variation in water levels. Using the algorithm proposed in [38], we estimated the skeleton storage coefficient S_k and the time delay τ of the deformation with respect to the head changes at each well station and converted the vertical surface deformation Δd_{up} into head changes Δh as $\Delta h(t) = \Delta d_{\text{up}}(t + \tau)/S_k$. We compared our results with the previously published results [31].

B. Greater Houston Area

The Greater Houston area, located on the Gulf Coastal plain, has experienced extensive land subsidence due to excessive groundwater pumping [40], [41]. A substantial proportion of this area is covered by dense vegetation, and InSAR phase measurements typically suffer severe decorrelation. We processed 93 C-band Sentinel-1A scenes (Path 143 and Frame 192) acquired between February 01, 2017 and February 22, 2020 [Fig. 4(b)]. We formed all 4278 multilooked interferograms (100 m-by-100 m pixel spacing), and we chose the Global Positioning System (GPS) station UHL1, where little vertical deformation was observed (<1 mm/year), as the reference location for all the interferograms. Similar to the SLV case, we selected PS pixels based on the phase similarity algorithm. We defined Ω_k as the PS set associated with the kth reference SLC scene. The common PS pixels in

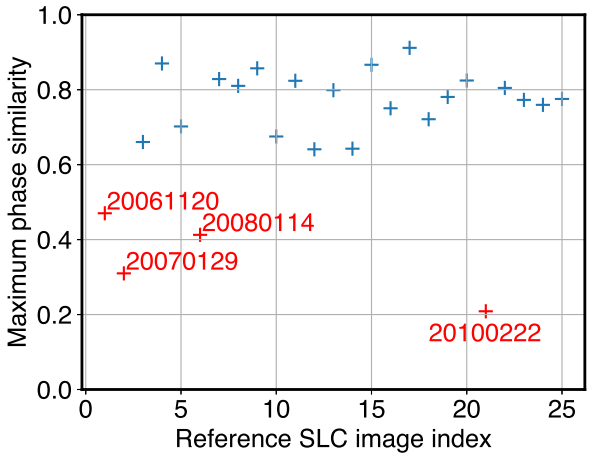

Fig. 5. Example of how the maximum phase similarity at a radar pixel (6) varies based on the choice of the reference SLC image. The horizontal axis represents the chronological indices (1–25) of the 25 Envisat SLC images used in the SLV test case. As our PS selection algorithm identifies a radar pixel as PS only if its maximum phase similarity is greater than a certain threshold (0.6 in this example), this pixel is not selected as PS when the Envisat SAR images acquired on November 20, 2006, January 29, 2007, January 14, 2008, and February 22, 2010 are used as the reference image (highlighted as red plus signs).

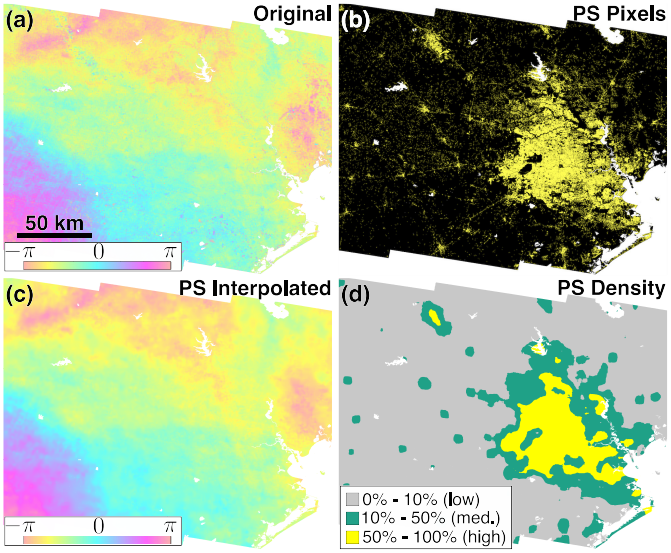

Fig. 6. (a) 12-day Sentinel-1 interferogram (January 03, 2018–January 15, 2018) over the Greater Houston area. Water bodies were masked out. (b) PS pixels (marked in yellow) identified using the phase similarity algorithm. (c) PS-interpolated interferogram. InSAR phase measurements at non-PS pixels can be reconstructed using phase measurements at PS pixels. (d) PS density calculated as the percentage of PS pixels within a 51 × 51 window centered at each pixel. (Gray) Low PS density (0%–10%). (Green) Medium PS density (10%–50%). (Yellow) High PS density (50%–100%).

Ω_k and Ω_l (or $\Omega_k \cap \Omega_l$) were considered as the valid PS pixels for the interferogram formed using the kth and the lth SLCs. We also compared the phase similarity algorithm and the MLE algorithm based on the quality of the interpolated interferograms. To implement the MLE algorithm, we used the Sentinel-1 scene acquired on December 17, 2018 as the reference scene to maximize the total InSAR phase correlation of the common reference interferograms.

We interpolated and unwrapped all 4278 interferograms using PS pixels selected by the phase similarity algorithm. We calculated the phase unwrapping error of each interpolated interferogram using (9), which ranges from 0 for coherent interferograms to more than 150 000 rad for severely decorrelated interferograms. We excluded 2969 interferograms with phase unwrapping errors larger than 10 000 rad. We removed a linear phase ramp from each of the remaining 1309 interferograms, and we excluded InSAR phase measurements corrupted by extreme tropospheric noise using an outlier removal algorithm [42]. We used a linear deformation model and solved for the average LOS surface deformation rate between 2017 and 2020 at each radar pixel [39]. As a control experiment, we estimated the LOS surface deformation rate from the original 1309 multilooked interferograms using phase measurements at both PS and non-PS pixels without PS interpolation. To evaluate the algorithm performance, we compared the surface deformation time series recorded at 93 permanent GPS stations [43] with our InSAR results. We projected GPS east, north, and up deformation time series to the radar LOS direction and estimated the average LOS surface deformation rate over the study period using the median interannual difference adjusted for skewness (MIDAS) algorithm [44].

IV. Results

A. PS Identification and Phase Reconstruction

Fig. 6(a) shows a 12-day Sentinel-1 interferogram (January 03, 2018–January 15, 2018) over the Greater Houston area. We identified PS pixels using the phase similarity algorithm [Fig. 6(b)]. Because the temporal baseline of the January 03, 2018–January 15, 2018 interferogram is short, there are very few phase decorrelation artifacts at both PS and non-PS pixels. We calculated the PS density as the percentage of PS pixels within a 51 pixel × 51 pixel window centered at each pixel [Fig. 6(d)]. Overall, the estimated PS density ranges from less than 1% over densely vegetated areas to more than 95% over urban areas near Downtown Houston. The PS-interpolated interferogram [Fig. 6(c)] and the original interferogram [Fig. 6(a)] show very few differences. This suggests that it is feasible to accurately reconstruct coherent InSAR phase measurements at non-PS pixels through an interpolation between PS pixels even in areas with very low PS density. This is because surface deformation and tropospheric noise signatures often vary slowly in space, which can be reconstructed using a small number of high-quality radar pixels based on the Nyquist sampling theorem.

To further demonstrate this finding, we processed a decorrelated 672-day Sentinel-1 interferogram (January 03, 2018–November 06, 2019) over the same area [Fig. 7(a)]. Because the temporal baseline of this interferogram is long, InSAR phase measurements are completely decorrelated at non-PS pixels. We compared the PS-interpolated interferogram [Fig. 7(c)] and the original interferogram with additional ten looks in both the dimensions [Fig. 7(b)]. While the additional looks can restore phase fringe patterns similar to PS interpolation, the multilooked phase measurements are much noisier over areas with low PS density (<10%). This is because multilooking averages the phase measurements at both PS and non-PS pixels to reduce the spatially incoherent phase noise. The phase noise reduction is less effective when non-PS pixels constitute the majority of local pixels. In contrast, our interpolation algorithm computes the weighted average phase of high-quality PS pixels identified by the phase similarity

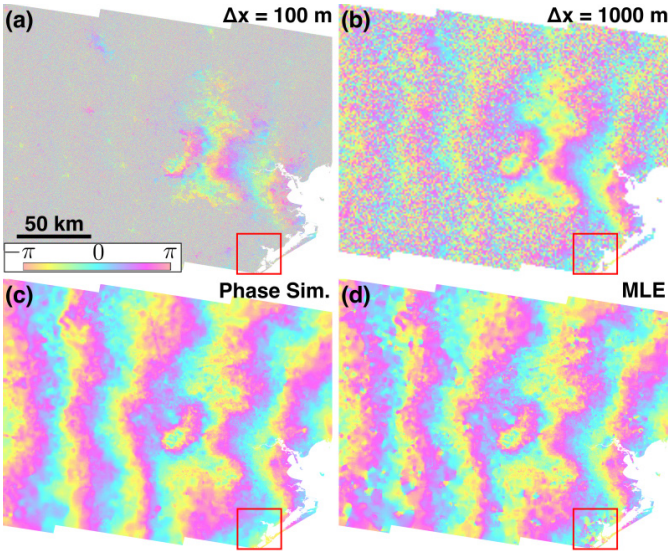

Fig. 7. (a) 672-day Sentinel-1 interferogram (January 03, 2018–November 06, 2019) over the Greater Houston area (100-m pixel spacing). (b) Same interferogram with additional 10 looks in both dimensions (1000-m pixel spacing). (c) Interpolated interferogram using PS pixels identified by the phase similarity algorithm. (d) Interpolated interferogram using PS pixels identified by the MLE algorithm. Here, we set the PS threshold as SCR >1, so that both the algorithms detect a similar number of PS pixels. The coastal region outlined in red is magnified in Fig. 8.

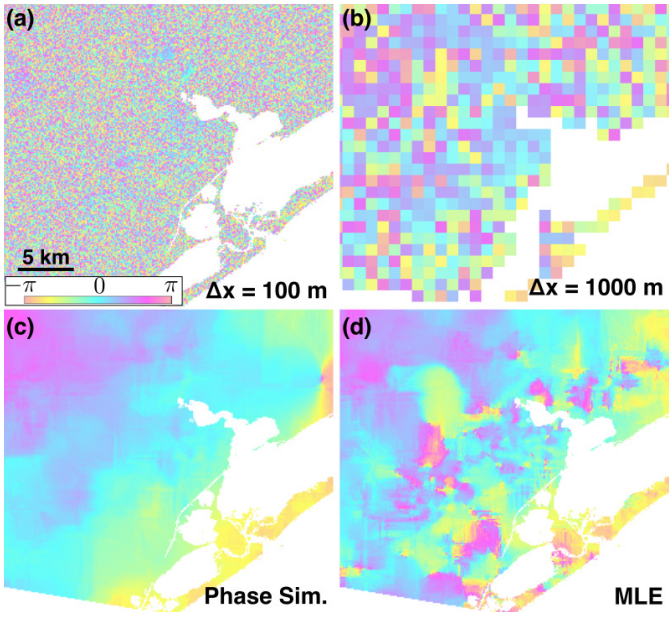

Fig. 8. (a) InSAR phase measurements of the original multilooked interferogram (100-m pixel spacing) over a coastal region outlined in red in Fig. 7. (b) InSAR phase measurements of the same interferogram with additional ten looks in both the dimensions (1000 m pixel spacing). (c) Interpolated InSAR phase measurements based on phase similarity PS identification. (d) Interpolated InSAR phase measurements based on MLE PS identification. The phase similarity algorithm results in fewer discontinuous artifacts in the reconstructed InSAR phase than the MLE algorithm.

algorithm, which can substantially reduce the spatially incoherent noise.

We compared the PS identification accuracy of our phase similarity algorithm and the MLE algorithm. Fig. 7(c) and (d) shows the interpolated interferograms based on PS pixels identified from these two algorithms. While both the interferograms show similar phase patterns, the phase similarity algorithm generates fewer interpolation artifacts (see the zoomed-in area in Fig. 8) and a smaller phase unwrapping error (1556.7 rad versus 9791.8 rad). Note that we set the SCR threshold so that the MLE algorithm selects approximately the same number of PS pixels as the phase similarity algorithm. While a higher SCR threshold reduces the false positive rate and interpolation artifacts, it also reduces the number of identified PS pixels and PS density. Our algorithm performs better because it can detect more PS pixels without compromising the detection accuracy.

B. InSAR Deformation Results Over the SLV

To mitigate vegetation decorrelation artifacts, Chen et al. [31] used the MLE algorithm to identify PS pixels. One limitation of the MLE algorithm is that it produced false positive PS pixels that display very different phases from nearby true PS pixels. These false positive PS pixels caused visible interpolation artifacts and phase unwrapping errors, especially in interferograms with longer temporal or perpendicular spatial baselines. For this reason, Chen et al. [31] only interpolated 186 out of 300 Envisat interferograms based on a maximum temporal and perpendicular spatial baselines of 600 days and 1000-m threshold. They further excluded 51 interferograms that contain visible interpolation artifacts from the InSAR time series analysis. Because none of the remaining 135 interferograms was generated using SLC scenes acquired on January 29, 2007 or January 14, 2008, there were two missing estimates in the InSAR-derived head time series.

In this study, we used the phase similarity algorithm to select PS pixels. This algorithm was designed to exclude the MLE false positive PS pixels without visual inspection and manual intervention. For example, Fig. 9(a) and (b) shows an Envisat interferogram (November 20, 2006–September 15, 2008) over U.S. Route 285, a highway across the SLV. The MLE algorithm selected these highway pixels as PS pixels, because their phases are stable over time. However, there are visible phase differences between these highway PS pixels and barren land PS pixels, which are mainly due to scattering property variations rather than actual deformation signals [Fig. 9(e)]. These highway pixels are considered as false positives, because they can lead to interpolation artifacts and phase unwrapping errors [Fig. 9(f)]. These artifacts are not observed in the interferograms reconstructed by the phase similarity algorithm [Fig.9 (c) and (d)]. The superiority of the phase similarity algorithm made it possible to repair 87 (∼65% more) interferograms that were previously excluded in [31]. For example, Fig. 10(a) shows a severely decorrelated Envisat interferogram (November 20, 2006–March 24, 2008) over SLV. The phase unwrapping error of the MLE results is 5932.0 rad [Fig. 10(d)], and the interferogram was not used in the previous study. In contrast, the phase unwrapping error of the phase similarity results is ten times smaller (511.1 rad), and the reconstructed interferogram meets the quality requirement for time series analysis.

To further validate that our algorithm produces high-quality interferograms, we estimated the seasonal deformation signals by averaging the interferograms that span the groundwater

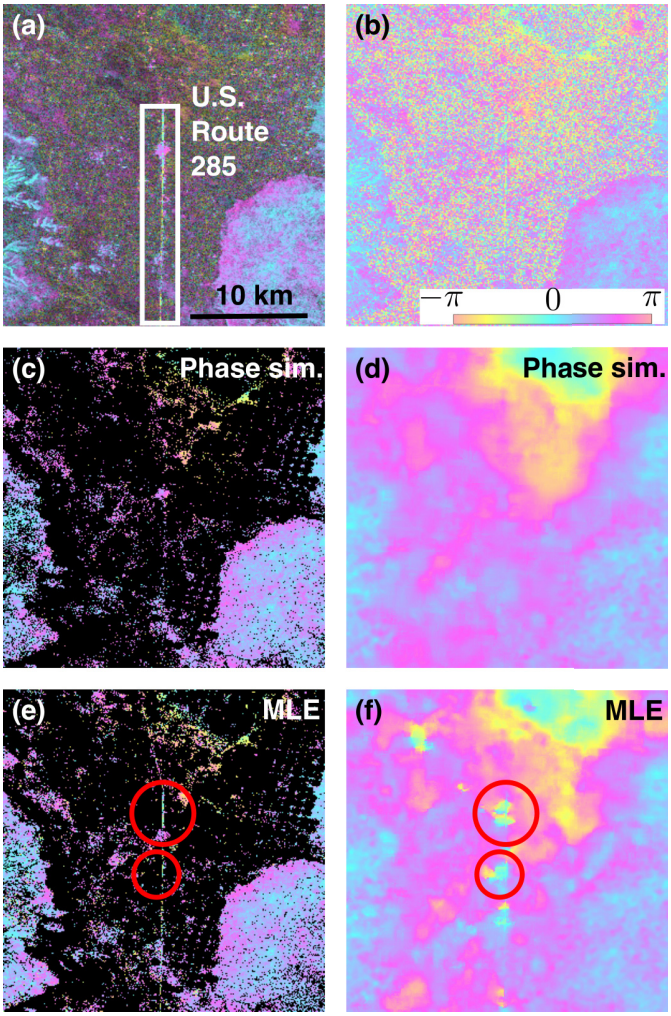

Fig. 9. (a) Envisat interferogram (November 20, 2006–September 15, 2008) over the SLV, Colorado. InSAR amplitude measurements are overlaid with InSAR phase measurements. The bright line in the white box corresponds to U.S. Route 285, a highway across the state of Colorado. (b) InSAR phase measurements of the interferogram shown in (a) without the amplitude layer. (c) PS pixels (colored by their InSAR phases) identified by the phase similarity PS selection algorithm. (d) Interpolated interferogram using PS pixels shown in (c). (e) PS pixels (colored by their InSAR phases) identified by the MLE algorithm with SCR >1.5. False positive pixels along U.S. Route 285 are circled in red. InSAR phase values at these highway pixels differ from nearby PS pixels in natural terrains by $\sim \pi$ rad. These phase differences are due to the differences in scattering mechanisms between concrete and natural surfaces rather than surface deformation. (f) Interpolated interferogram using PS pixels shown in (e). False positive PS pixels along US. Route 285 caused phase artifacts as circled in red.

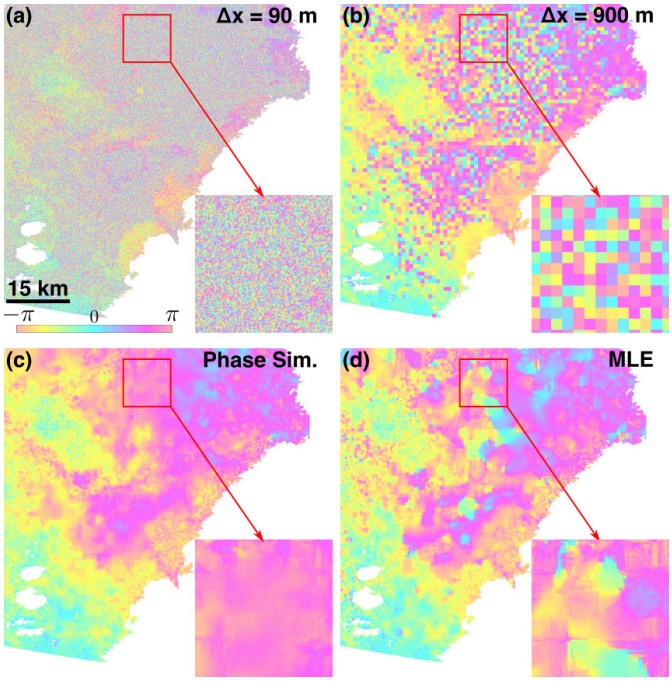

Fig. 10. (a) Envisat interferogram (November 20, 2006–March 24, 2008) over the SLV, Colorado. The pixel size of this multilooked interferogram is 90 m. The area in the red box corresponds to highly decorrelated agricultural fields with low PS density. (b) Spatial phase correlation is improved in the interferogram with additional ten looks (900-m pixel spacing), but InSAR phases are still noisy over low PS density areas. (c) Interpolated InSAR phase based on the PS pixels identified by the phase similarity PS selection algorithm, which are coherent within the red box. (d) Interpolated InSAR phase based on MLE PS identification (with SCR >3), which shows visible phase artifacts.

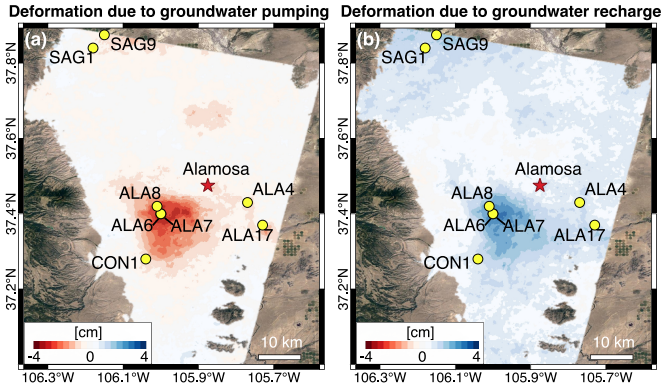

Fig. 11. Average seasonal (a) subsidence and (b) uplift due to groundwater pumping and recharge over the SLV between November 2006 and July 2010. Yellow circles mark the locations of eight confined aquifer wells with either seasonal subsidence or uplift greater than 1 cm.

pumping and recharge seasons (listed in Table I). The resulting seasonal subsidence and uplift maps [Fig. 12(a) and (b)] are consistent with the previous study. In regions where the seasonal deformation signal is greater than 1 cm, the Root-Mean-Square (RMS) differences between the InSAR head time series and the well head measurements range from 0.61 to 0.92 m (Fig. 12), which is comparable to [31]. The additional 87 repaired interferograms allowed us to recover deformation signals at two missing SAR dates. Many of these interferograms have long temporal baselines and thus larger long-term deformation signals, which are key for constraining the long-term deformation rate. For the case of SLV, the improved InSAR-estimated head time series suggest that head levels were stable and little long-term water storage loss occurred over the study period. These results are especially important for the management of groundwater in the SLV, where the Confined Aquifer Rules decision requires that the head in confined aquifers be maintained within the range of levels measured between 1978 and 2000 [45].

C. InSAR Deformation Results Over the Greater Houston Area

Fig. 13(a) and (b) shows the average InSAR LOS deformation velocity estimates (February 2017 to February 2020)

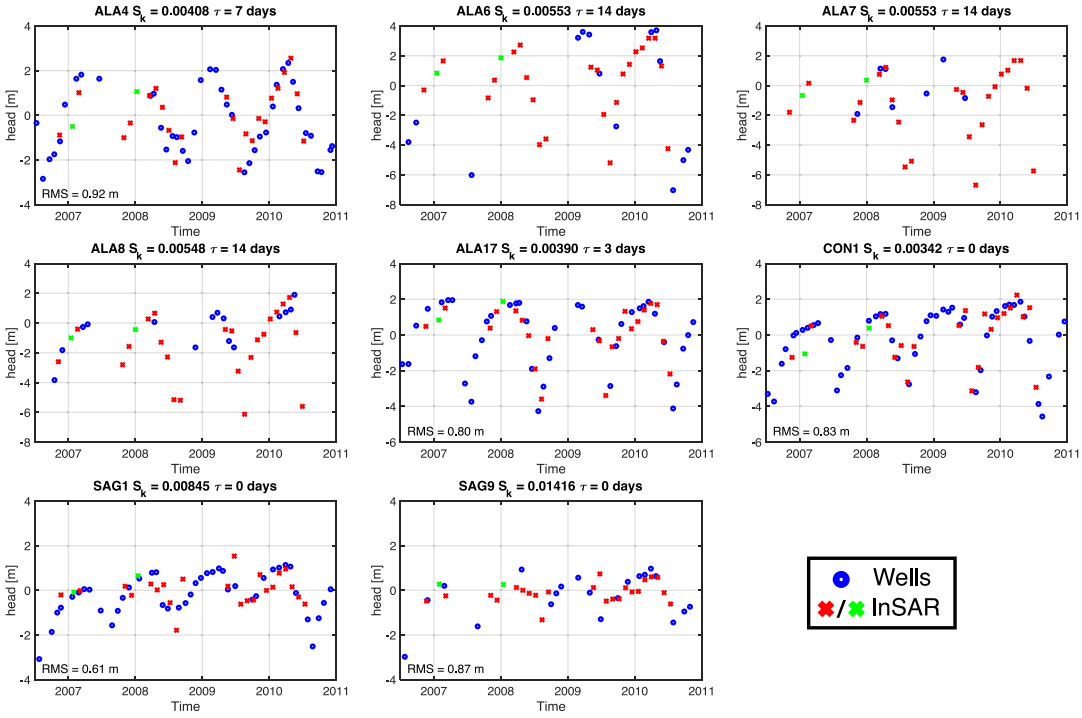

Fig. 12. Hydraulic head time series between November 2006 and July 2010 at eight confined aquifer wells shown in Fig. 11 as derived from InSAR (red and green) and in situ data (blue). The two previous missing dates (January 29, 2007 and January 14, 2008) [31] are highlighted in green. We were able to recover these two time samples by repairing 87 decorrelated interferograms that were excluded in the previous study. Here, RMS represents the root-mean-square difference between the InSAR head estimates and well head measurements. The RMS differences for ALA6, ALA7, and ALA8 were not calculated because there are not enough well samples to perform interpolation.

TABLE I
INTERFEROGRAMS USED FOR ESTIMATING AVERAGE SEASONAL DEFORMATION

Pumping Season	Recharge Season
20080324-20090727	20071105-20080428
20080602-20080915	20080811-20090622
20090518-20090831	20090727-20100329
20091214-20100712	20091005-20100222

over the high PS density area (>50%) as derived from the original and PS-improved interferograms. Overall, the two deformation maps show consistent InSAR deformation patterns. Using 44 GPS time series as ground truth, the root-mean-square error (RMSE) of the InSAR LOS deformation rate estimates is 0.15 and 0.13 cm/yr before and after PS processing, respectively [Fig. 14(a)]. Because there are 70.7% PS pixels in this region on average, phase decorrelation artifacts and unwrapping errors are minimal. It is not necessary to perform PS analysis in this case, given that the two solutions were derived from two similar sets of high-quality pixels.

In contrast, the average InSAR LOS deformation velocity map derived from the PS-improved interferograms reveals widespread subsidence patterns over the low PS density area (<50%) that are otherwise undetectable [Fig. 13(c) and (d)]. For example, the subsidence patterns (up to 0.5 cm/yr) within a region outlined in red are only present in the PS-improved solution [Fig. 13(e) and (f)]. Because the phase vector of a decorrelated pixel is random, fitting a linear deformation model to decorrelated InSAR observations tends to yield a near-zero deformation rate estimate when the vector size is sufficiently large. This means that decorrelation noise can lead to a systematic underestimation of surface deformation rate. As shown in Fig. 14(b), while a majority of GPS stations suggest that LOS deformation of a few millimeters per year is present, decorrelated InSAR observations incorrectly indicate that LOS deformation rates at these locations are near zero. Our PS processing algorithm only uses high-quality InSAR measurements with minimal decorrelation noise, and thus can reconstruct the true surface deformation rate without this systematic bias. In the Houston case, the systematic underestimation is on the order of a few millimeters per year and relatively small. This is because coastal processes along the Gulf Coast typically only lead to millimeter-level deformation signals. We emphasize that it is important to capture these subtle deformation signals to evaluate future flooding risks along coastal regions, because the current projected sea-level rise estimates are in the order of a few millimeters per year as well [46]. In case that a large deformation signal (e.g., 10 cm/yr) is present, decorrelated InSAR observations still tend to yield a near-zero deformation rate estimate. Therefore, the magnitude of the systematic underestimation is on the same order as the signal of interest over severely decorrelated regions. We conclude that it is critical to use PS techniques to select high-quality InSAR measurements for time series analysis over areas with low or very low PS density.

V. DISCUSSIONS

A. Interferogram-Specific PS Selection

One important design of our algorithm is that a pixel can be marked as a PS pixel in one interferogram, while the same

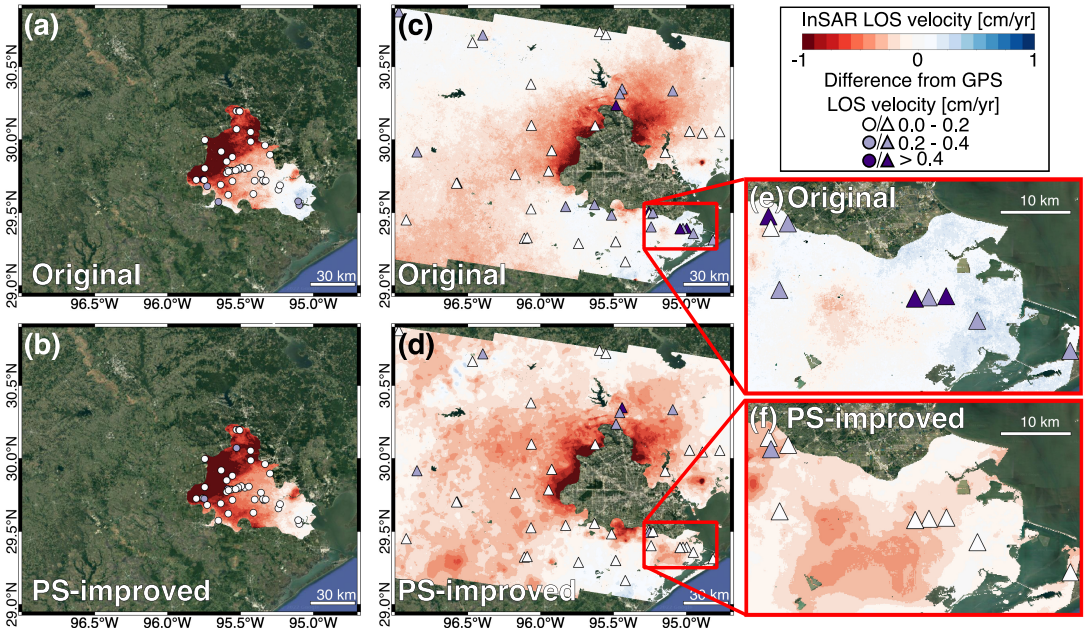

Fig. 13. (a) and (b) Average Sentinel-1 LOS deformation velocity map (between February 2017 and February 2020) over the high PS density area (>50%) as derived from the original and PS-improved interferograms. Circles represent the locations of 44 independent GPS validation stations. The GPS stations are color-coded to show the absolute differences between the InSAR- and GPS-derived LOS deformation rates. White circles indicate differences within 0.2 cm/yr. (c) and (d) Average Sentinel-1 LOS deformation velocity map (between February 2017 and February 2020) over the low PS density area (<50%) as derived from the original and PS-improved interferograms. Triangles represent the locations of 49 GPS stations, which are color-coded based on the same rule as in (a) and (b). Red boxes outline the regions where the original and PS-improved deformation maps exhibit substantial differences. The red boxes on the bottom right corner of (c) and (d) were magnified in (e) and (f), respectively.

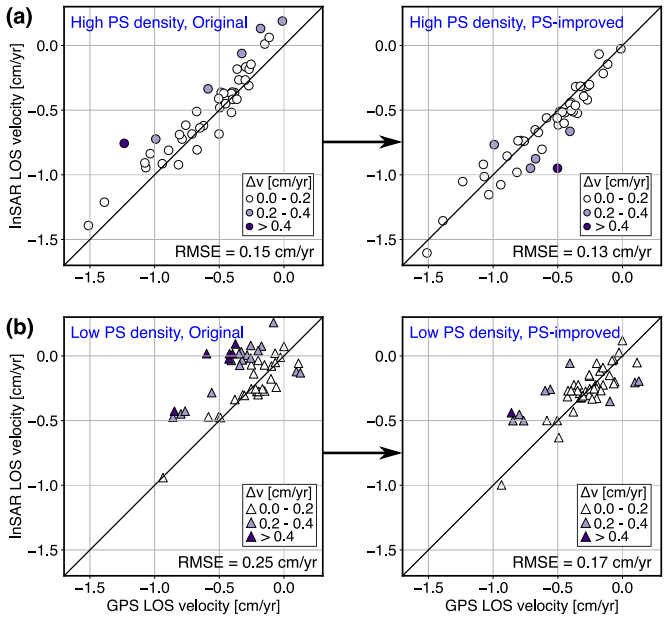

Fig. 14. Scatter plots of colocated GPS and InSAR LOS deformation rate over (a) high PS density area (circles) and (b) low PS density area (triangles) shown in Fig. 13. Circles and triangles are color-coded to show the absolute differences (Δv) between the InSAR- and GPS-derived LOS deformation rates.

pixel can be marked as a non-PS in another interferogram. This is a reasonable design, because: 1) our goal is to select as many high-quality InSAR phase measurements as possible for surface deformation time series analysis and 2) the quality of SAR images and their corresponding interferograms can vary significantly. As described in Section II-A, given K SLC images $S_1, \ldots, S_k$, we use each of them as the reference image and select K different PS sets $\Omega_1, \ldots, \Omega_K$. If we form an interferogram using S_k and S_l, the quality of this interferogram is determined by the noise level of S_k and S_l, and not the noise level of the remaining $K-2$ SAR images. Based on this fact, we use the intersection of Ω_k and Ω_l ($\Omega_k \cap \Omega_l$) as the valid PS set for this interferogram. As an example, Fig. 15(a)–(d) shows the identified PS pixels for two Envisat interferograms over the SLV. The number of detected PS pixels in the interferogram April 28, 2008–June 02, 2008 is approximately three times more than in the interferogram January 29, 2007–April 28, 2008. As shown in Fig. 15(e)–(j), the PS set size differences are mainly due to the relatively high phase decorrelation noise in the SAR scene January 29, 2007. In contrast, previous PS algorithms [15], [20], [21] usually select a single PS set based on an optimized set of common reference interferograms that maximizes PS detections. This can lead to substantially higher false positive rates for decorrelated interferograms and larger uncertainties in surface deformation estimates. We conclude that it is necessary to select a unique PS set for each interferogram in low PS density nature terrains to keep both the false positive and false negative detection rates low.

B. Choice of Phase Similarity Thresholds

In our algorithm, we use a median phase similarity threshold $s_{\text{med,thr}}$ to remove false positive PS candidates and a probability threshold α to determine the maximum phase similarity threshold $s_{\text{max,thr}}$ and recover false negative PS pixels. In this section, we demonstrate how the choices of $s_{\text{med,thr}}$ and α affect the PS selection results using 92 Sentinel-1 interferograms formed

TABLE II
NUMBER OF SELECTED PS PIXELS AS A FUNCTION OF $s_{\text{med,thr}}$

Threshold ($s_{\text{med,thr}}$)	0	0.1	0.2	0.3	0.4	0.5
False positive PS	231	632	1,279	2,701	6,762	25,571
False negative PS	153,024	153,212	153,688	155,162	159,571	179,750
Net false positive PS	125	293	422	539	552	544
Finally selected PS	405,247	405,034	404,863	404,915	405,263	406,633

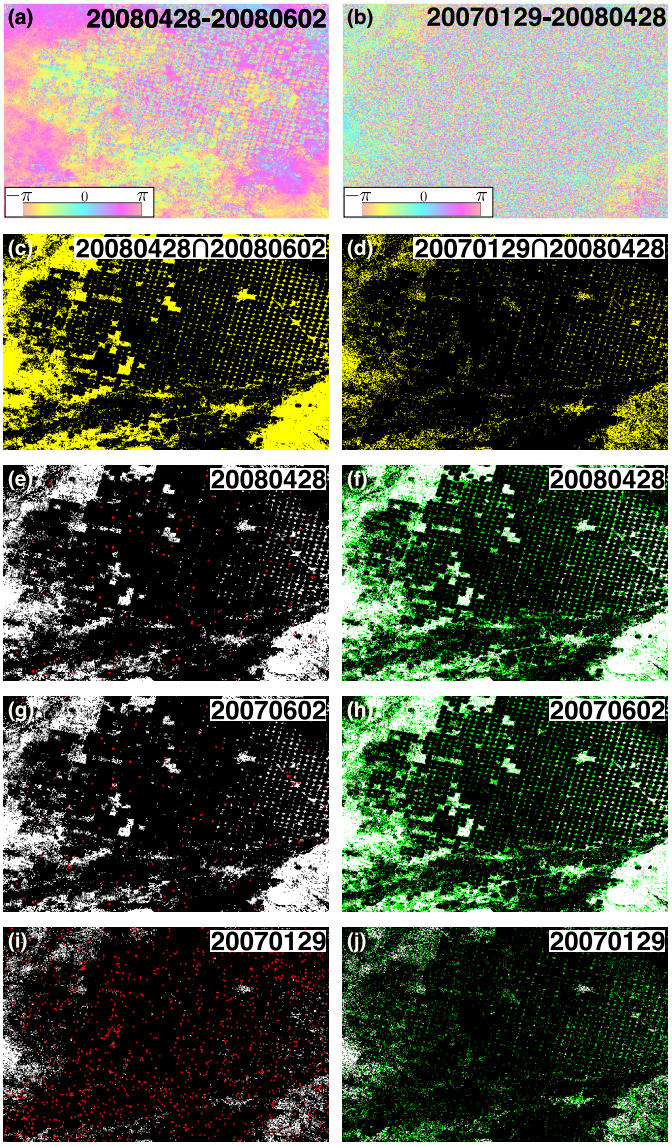

Fig. 15. Two Envisat interferograms (a) April 28, 2008–June 02, 2008 (b) January 29, 2007–April 28, 2008 over an agricultural area in the SLV, Colorado. (c) 48 065 identified PS pixels for the interferogram in panel (a). (d) 16 888 identified PS pixels for the interferogram in panel (b). (e), (g), and (i) Preliminary PS candidate pixels for three SAR acquisitions April 28, 2008, June 02, 2008, and January 29, 2007. False positive pixels detected by the phase similarity algorithm are shown in red. (f), (h), and (j) Final selected PS pixels for the same three SAR acquisitions. False negative PS pixels detected by the phase similarity algorithm are shown in green. Here, the PS set of an interferogram is defined as the intersection of PS sets of two corresponding SAR scenes.

with a common reference Sentinel-1 SAR image acquired on January 03, 2018 over the Houston area.

We first fixed α to 1% and performed PS selection using different $s_{\text{med,thr}}$ ranging from 0 to 0.5 with an increment of 0.1.

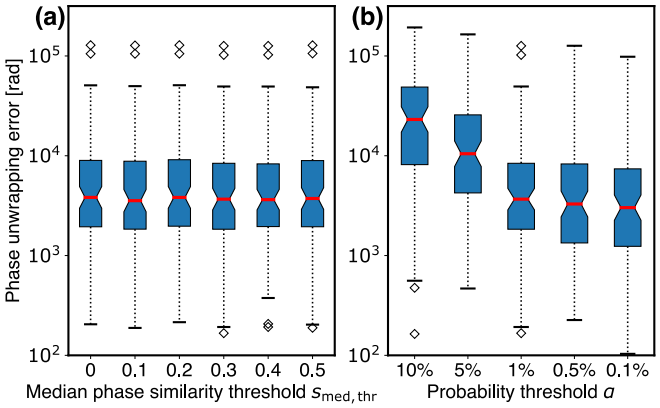

Fig. 16. (a) Phase unwrapping errors as a function of the median phase similarity threshold $s_{\text{med,thr}}$. (b) Phase unwrapping errors as a function of the probability threshold α. The box extends from the first quartile to the third quartile of the phase unwrapping errors, with a red line showing the median. The whiskers extend from the box by 1.5 times the range of the interquartile range. Diamonds show the flier points that are past the end of the whiskers. Here, the analysis is based on the phase unwrapping errors of 92 interferograms formed with respect to the Sentinel-1 scene acquired on January 03, 2018 over the Greater Houston area.

Table II shows the numbers of detected false positive, false negative, and final PS pixels as a function of $s_{\text{med,thr}}$. While the number of false positive PS pixels increases as $s_{\text{med,thr}}$ increases, the total number of selected PS pixels does not vary much. This indicates that using a high $s_{\text{med,thr}}$ caused an excessive removal of false positive PS pixels, and these removed PS pixels were recovered during the identification of false negative PS pixels. By excluding these pixels that were counted as both false positives and false negatives, we computed a set of net false positive PS pixels. The number of net false positive PS pixels increases from 125 to 539 as $s_{\text{med,thr}}$ increases from 0 to 0.3, and remains stable as we further increase $s_{\text{med,thr}}$ (Table II). Therefore, a median phase similarity threshold greater or equal to 0.3 is necessary for removing false positive PS pixels in this case. To further evaluate the quality of PS selection as a function of $s_{\text{med,thr}}$, we used the PS set corresponding to $s_{\text{med,thr}} = 0$ to interpolate all the 92 common reference interferograms and calculated their unwrapping errors. We then repeated the same interpolation and calculation using the PS sets corresponding to $s_{\text{med,thr}}$ equal 0.1, 0.2, 0.3, 0.4, and 0.5, respectively. We found that the distribution of unwrapping errors is very similar for different $s_{\text{med,thr}}$ [Fig. 16(a)]. The PS selection quality is not sensitive to $s_{\text{med,thr}}$ due to the small number of false positive PS pixels in the preliminary PS candidate set. We finally set $s_{\text{med,thr}} = 0.3$ in our studies because it is large enough to remove false positive PS pixels and small enough to limit the excessive removal of PS candidates.

TABLE III
NUMBER OF SELECTED PS PIXELS AS A FUNCTION OF α

Threshold (α)	10%	5%	1%	0.5%	0.1%
$s_{\max,\text{thr}}$	0.389	0.412	0.471	0.523	0.712
Finally selected PS	511,840	465,735	404,915	364,165	269,320

Next, we fixed the median phase similarity threshold $s_{\text{med,thr}}$ to 0.3 and selected PS pixels using different probability thresholds α. The corresponding maximum phase similarity threshold $s_{\max,\text{thr}}$ and the number of selected PS pixels are summarized in Table III. Similar to the test on the median phase similarity threshold, we used the PS sets calculated from different probability thresholds to interpolate the 92 common reference interferograms and calculated their unwrapping errors [Fig. 16(b)]. The median of phase unwrapping errors decreases by 84% from 23104.9 to 3674.3 rad as the probability threshold α changes from 10% to 1%. A further decrease in α only slightly mitigates the phase unwrapping errors but substantially reduces the number of detected PS pixels (Table III). As a result, we chose 1% as the probability threshold in our test cases.

While the thresholds $s_{\text{med,thr}}$ and α were selected based on the analysis of 92 common reference Sentinel-1 interferograms, we were able to use the same threshold values to process the remaining C-band Sentinel-1 Houston interferograms and C-band Envisat SLV interferograms and achieve similar performance. We found that it is not necessary to adjust these thresholds if sufficient PS pixels were identified. In the case that additional PS pixels are needed to reconstruct the spatial coherent phase patterns, a similar analysis as described in this section can be performed to determine the optimized thresholds.

VI. CONCLUSION

In this study, we developed a new PS identification algorithm based on the phase similarity between nearby radar pixels. Our algorithm is based on the assumption that the spatially coherent phase terms (e.g., deformation and atmospheric phases) vary smoothly and slowly in space. In this scenario, the spatially incoherent decorrelation noise is the major factor that reduces the phase similarity between nearby radar pixels. While this assumption is valid in most InSAR case studies, deformation or tropospheric noise signatures that vary rapidly in space may present in some interferograms. This can also lead to a phase similarity reduction between nearby radar pixels, and thus increase the false negative PS identification rate. In addition, when the PS density is too low to adequately sample the high-frequency tropospheric noise or deformation signal signatures, PS interpolation may suffer from spatial aliasing artifacts. Future work will focus on improving the robustness of both PS selection and phase interpolation in the presence of spatially coherent phase components that vary rapidly in space.

ACKNOWLEDGMENT

Envisat SAR imagery over the San Luis Valley (SLV) is accessible through the UNAVCO Data Center SAR archive at https://www.unavco.org/data/sar/sar.html. The SLV confined aquifer well data are available through the SLV Well and Water-Level Database https://www.prinmath.com/rgwcd/loc/cawslist.htm).

Sentinel-1 SAR imagery over the Greater Houston area can be downloaded from the Alaska Satellite Facility at https://search.asf.alaska.edu. GPS data were processed by the Nevada Geodetic Laboratory (http://geodesy.unr.edu/magnet.php). A list of GPS stations used in this study can be found in the supplementary materials.

The code for implementing the phase similarity and PS interpolation algorithm will be available through GitHub (https://github.com/orgs/UT-Radar-Interferometry-Group).

REFERENCES

[1] R. Bamler and P. Hartl, "Synthetic aperture radar interferometry," *Inverse Problems*, vol. 14, no. 4, pp. 1–54, Aug. 1998, doi: 10.1088/0266-5611/14/4/001.

[2] P. Rosen et al., "Synthetic aperture radar interferometry," *Proc. IEEE*, vol. 88, no. 3, pp. 333–382, Mar. 2000.

[3] D. Massonnet et al., "The displacement field of the Landers earthquake mapped by radar interferometry," *Nature*, vol. 364, no. 6433, pp. 138–142, 1993, doi: 10.1038/364138a0.

[4] G. Peltzer and P. Rosen, "Surface displacement of the 17 May 1993 Eureka Valley, California, earthquake observed by SAR interferometry," *Science*, vol. 268, no. 5215, pp. 1333–1336, 1995, doi: 10.1126/science.268.5215.1333.

[5] D. L. Galloway et al., "Detection of aquifer system compaction and land subsidence using interferometric synthetic aperture radar, antelope valley, mojave desert, California," *Water Resour. Res.*, vol. 34, no. 10, pp. 2573–2585, Oct. 1998, doi: 10.1029/98WR01285.

[6] Z. Lu and W. R. Danskin, "InSAR analysis of natural recharge to define structure of a ground-water basin, San Bernardino, California," *Geophys. Res. Lett.*, vol. 28, no. 13, pp. 2661–2664, Jul. 2001, doi: 10.1029/2000GL012753.

[7] M. E. Pritchard and M. Simons, "A satellite geodetic survey of large-scale deformation of volcanic centres in the central Andes," *Nature*, vol. 418, no. 6894, pp. 167–171, Jul. 2002, doi: 10.1038/nature00872.

[8] L. Liu, T. Zhang, and J. Wahr, "InSAR measurements of surface deformation over permafrost on the North Slope of Alaska," *J. Geophys. Res.*, vol. 115, no. 3, pp. 1–14, 2010, doi: 10.1029/2009JF001547.

[9] X. Hu, T. Wang, T. C. Pierson, Z. Lu, J. Kim, and T. H. Cecere, "Detecting seasonal landslide movement within the cascade landslide complex (Washington) using time-series SAR imagery," *Remote Sens. Environ.*, vol. 187, pp. 49–61, Dec. 2016. [Online]. Available: https://www.sciencedirect.com/science/article/pii/S0034425716303789

[10] J. Biggs and T. J. Wright, "How satellite InSAR has grown from opportunistic science to routine monitoring over the last decade," *Nature Commun.*, vol. 11, no. 1, p. 3863, Dec. 2020, doi: 10.1038/s41467-020-17587-6.

[11] X. Xu, D. T. Sandwell, and B. Smith-Konter, "Coseismic displacements and surface fractures from Sentinel-1 InSAR: 2019 ridgecrest earthquakes," *Seismolog. Res. Lett.*, vol. 91, no. 4, pp. 1979–1985, Jul. 2020, doi: 10.1785/0220190275.

[12] J. Chen et al., "Active layer freeze-thaw and water storage dynamics in permafrost environments inferred from InSAR," *Remote Sens. Environ.*, vol. 248, Oct. 2020, Art. no. 112007. [Online]. Available: https://www.sciencedirect.com/science/article/pii/S0034425720303771

[13] H. A. Zebker and J. Villasenor, "Decorrelation in interferometric radar echoes," *IEEE Trans. Geosci. Remote Sens.*, vol. 30, no. 5, pp. 950–959, Sep. 1992.

[14] A. Ferretti, C. Prati, and F. Rocca, "Nonlinear subsidence rate estimation using permanent scatterers in differential SAR interferometry," *IEEE Trans. Geosci. Remote Sens.*, vol. 38, no. 5, pp. 2202–2212, Sep. 2000.

[15] A. Hooper, H. Zebker, P. Segall, and B. Kampes, "A new method for measuring deformation on volcanoes and other natural terrains using InSAR persistent scatterers," *Geophys. Res. Lett.*, vol. 31, no. 23, pp. 1–5, Dec. 2004.

[16] A. Ferretti, A. Fumagalli, F. Novali, C. Prati, F. Rocca, and A. Rucci, "A new algorithm for processing interferometric data-stacks: SqueeSAR," *IEEE Trans. Geosci. Remote Sens.*, vol. 49, no. 9, pp. 3460–3470, Sep. 2011.

[17] A. Ferretti, C. Prati, and F. Rocca, "Permanent scatterers in SAR interferometry," *IEEE Trans. Geosci. Remote Sens.*, vol. 39, no. 1, pp. 8–20, Jan. 2001.
[18] S. Lyons and D. Sandwell, "Fault creep along the southern San Andreas from interferometric synthetic aperture radar, permanent scatterers, and stacking," *J. Geophys. Res., Solid Earth*, vol. 108, no. 1, pp. 1–24, Jan. 2003.
[19] F. J. Van Leijen, "Persistent scatterer interferometry based on geodetic estimation theory," Ph.D. dissertation, Dept. Geosci. Remote Sens., Delft Univ. Technol., Delft, The Netherlands, 2014.
[20] A. Hooper and H. A. Zebker, "Phase unwrapping in three dimensions with application to InSAR time series," *J. Opt. Soc. Amer. A, Opt. Image Sci.*, vol. 24, no. 9, pp. 2737–2747, Aug. 2007. [Online]. Available: http://josaa.osa.org/abstract.cfm?URI=josaa-24-9-2737
[21] P. Shanker and H. Zebker, "Persistent scatterer selection using maximum likelihood estimation," *Geophys. Res. Lett.*, vol. 34, no. 22, pp. 1–4, 2007, doi: 10.1029/2007GL030806.
[22] S. Huang and H. A. Zebker, "Persistent scatterer density by image resolution and terrain type," *IEEE J. Sel. Topics Appl. Earth Observ. Remote Sens.*, vol. 12, no. 7, pp. 2069–2079, Jul. 2019.
[23] K. Goel and N. Adam, "A distributed scatterer interferometry approach for precision monitoring of known surface deformation phenomena," *IEEE Trans. Geosci. Remote Sens.*, vol. 52, no. 9, pp. 5454–5468, Sep. 2014.
[24] X. Lv, B. Yazici, M. Zeghal, V. Bennett, and T. Abdoun, "Joint-scatterer processing for time-series InSAR," *IEEE Trans. Geosci. Remote Sens.*, vol. 52, no. 11, pp. 7205–7221, Nov. 2014.
[25] A. M. Guarnieri and S. Tebaldini, "On the exploitation of target statistics for SAR interferometry applications," *IEEE Trans. Geosci. Remote Sens.*, vol. 46, no. 11, pp. 3436–3443, Nov. 2008.
[26] M. Costantini, S. Falco, F. Malvarosa, and F. Minati, "A new method for identification and analysis of persistent scatterers in series of SAR images," in *Proc. IEEE Int. Geosci. Remote Sens. Symp. (IGARSS)*, Jul. 2008, pp. 449–452.
[27] M. Costantini, S. Falco, F. Malvarosa, F. Minati, F. Trillo, and F. Vecchioli, "Persistent scatterer pair interferometry: Approach and application to COSMO-SkyMed SAR data," *IEEE J. Sel. Topics Appl. Earth Observ. Remote Sens.*, vol. 7, no. 7, pp. 2869–2879, Jul. 2014.
[28] J. Lien, "Partially correlated persistent scatterer theory and techniques for radar interferometry," Ph.D. dissertation, Dept. Elect. Eng., Stanford Univ., Stanford, CA, USA, 2016.
[29] P. Segall, *Earthquake and Volcano Deformation*. Princeton, NJ, USA: Princeton Univ. Press, 2010.
[30] N. Adam, B. Kampes, M. Eineder, J. Worawattanamateekul, and M. Kircher, "The development of a scientific permanent scatterer system," in *Proc. Joint ISPRS/EARSeL Workshop High Resolution Mapping Space*, 2003, pp. 1–6.
[31] J. Chen, R. Knight, and H. A. Zebker, "The temporal and spatial variability of the confined aquifer head and storage properties in the San Luis Valley, Colorado inferred from multiple InSAR missions," *Water Resour. Res.*, vol. 53, no. 11, pp. 9708–9720, 2017, doi: 10.1002/2017WR020881.
[32] F. Sica, A. Pulella, M. Nannini, M. Pinheiro, and P. Rizzoli, "Repeat-pass SAR interferometry for land cover classification: A methodology using Sentinel-1 short-time-series," *Remote Sens. Environ.*, vol. 232, Oct. 2019, Art. no. 111277. [Online]. Available: https://www.sciencedirect.com/science/article/pii/S0034425719302962
[33] K. Wang, J. Chen, A. Kiaghadi, and C. Dawson, "A new algorithm for land-cover classification using PolSAR and InSAR data and its application to surface roughness mapping along the Gulf coast," *IEEE Trans. Geosci. Remote Sens.*, vol. 60, pp. 1–15, 2022.
[34] J. Chen, H. A. Zebker, and R. Knight, "A persistent scatterer interpolation for retrieving accurate ground deformation over InSAR-decorrelated agricultural fields," *Geophys. Res. Lett.*, vol. 42, no. 21, pp. 9294–9301, Nov. 2015, doi: 10.1002/2015GL065031.
[35] C. W. Chen and H. A. Zebker, "Two-dimensional phase unwrapping with use of statistical models for cost functions in nonlinear optimization," *J. Opt. Soc. Amer. A*, vol. 18, no. 2, pp. 338–351, 2001. [Online]. Available: http://josaa.osa.org/abstract.cfm?URI=josaa-18-2-338
[36] J. A. Reeves, R. Knight, H. A. Zebker, W. A. Schreüder, P. S. Agram, and T. R. Lauknes, "High quality InSAR data linked to seasonal change in hydraulic head for an agricultural area in the San Luis Valley, Colorado," *Water Resour. Res.*, vol. 47, no. 12, pp. 1–14, Dec. 2011, doi: 10.1029/2010WR010312.
[37] J. A. Reeves, R. Knight, H. A. Zebker, P. K. Kitanidis, and W. A. Schreuder, "Estimating temporal changes in hydraulic head using InSAR data in the San Luis Valley, Colorado," *Water Resour. Res.*, vol. 50, no. 5, pp. 4459–4473, May 2014, doi: 10.1002/2013WR014938.
[38] J. Chen, R. Knight, H. A. Zebker, and W. A. Schreuder, "Confined aquifer head measurements and storage properties in the San Luis Valley, Colorado, from spaceborne InSAR observations," *Water Resour. Res.*, vol. 52, no. 5, pp. 3623–3636, May 2016, doi: 10.1002/2015WR018466.
[39] P. Berardino, G. Fornaro, R. Lanari, and E. Sansosti, "A new algorithm for surface deformation monitoring based on small baseline differential SAR interferograms," *IEEE Trans. Geosci. Remote Sens.*, vol. 40, no. 11, pp. 2375–2383, Nov. 2002.
[40] F. Qu et al., "Mapping ground deformation over Houston–Galveston, Texas using multi-temporal InSAR," *Remote Sens. Environ.*, vol. 169, pp. 290–306, Nov. 2015. [Online]. Available: https://www.sciencedirect.com/science/article/pii/S0034425715301152
[41] M. M. Miller and M. Shirzaei, "Land subsidence in Houston correlated with flooding from hurricane Harvey," *Remote Sens. Environ.*, vol. 225, pp. 368–378, May 2019. [Online]. Available: https://www.sciencedirect.com/science/article/pii/S0034425719301130
[42] S. Staniewicz et al., "InSAR reveals complex surface deformation patterns over an 80,000 km^2 oil-producing region in the Permian basin," *Geophys. Res. Lett.*, vol. 47, no. 21, pp. 1–10, Nov. 2020, doi: 10.1029/2020GL090151.
[43] G. Blewitt, W. Hammond, and C. Kreemer, "Harnessing the GPS data explosion for interdisciplinary science," *Eos*, vol. 99, p. 485, Sep. 2018.
[44] G. Blewitt, C. Kreemer, W. C. Hammond, and J. Gazeaux, "MIDAS robust trend estimator for accurate GPS station velocities without step detection," *J. Geophys. Res., Solid Earth*, vol. 121, no. 3, pp. 2054–2068, Mar. 2016, doi: 10.1002/2015JB012552.
[45] O. J. Kuenhold, "Confined aquifer new use rules for division. 3: Findings of fact, conclusions of law, judgement and decree," District Court, Water Division, Tech. Rep. 3, 2006. [Online]. Available: https://www.courts.state.co.us/Courts/Water/Division.cfm?Water_Division_ID=3
[46] W. Sweet et al., "Global and regional sea level rise scenarios for the United States: Updated mean projections and extreme water level probabilities along U.S. Coastlines," Nat. Ocean. Atmos. Admin., Nat. Ocean Service, NOAA Tech. Rep. NOS 01, 2022.

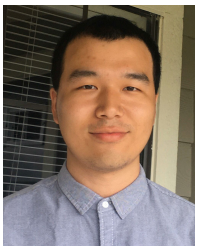

Ke Wang received the B.S. degree in physics from Nanjing University, Nanjing, China, in 2015, and the M.S. degree in engineering from Ecole Polytechnique, Palaiseau, France, in 2018. He is currently pursuing the Ph.D. degree in aerospace engineering with the University of Texas at Austin, Austin, TX, USA.

Since 2018, he has been a Research Assistant with the Radar Interferometry Group, University of Texas at Austin. His research interests include land-cover classification algorithms based on interferometric synthetic aperture radar (InSAR) data, InSAR processing, and InSAR time series analysis.

Mr. Wang is a Student Member of the American Geophysical Union.

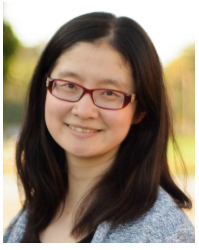

Jingyi Chen (Member, IEEE) received the B.S. degree in geophysics from the University of Science and Technology of China, Hefei, China, in 2008, and the M.S. degree in electrical engineering and the Ph.D. degree in geophysics from Stanford University, California, CA, USA, in 2012 and 2014, respectively.

She has more than ten years of experience in SAR/InSAR algorithm design for Earth science applications and she is currently an Assistant Professor of aerospace engineering with the University of Texas at Austin, Austin, TX, USA. Her group focuses on the development of new satellite, especially interferometric synthetic aperture radar (InSAR) techniques for Earth system science research.

Dr. Chen is a member of American Geophysical Union.